Magnetophoretic force and homogeneity optimization in multiplexed magnetic tweezers for microrheometry applications

Alejandro Rodriguez-Barroso [*], Guillermo Camacho, Oscar Martinez-Cano, Jose Rafael Morillas, Juan de Vicente

F2N2Lab, Magnetic Soft Matter Group and Excellence Research Unit 'Modeling Nature' (MNat), Department of Applied Physics, Faculty of Sciences, University of Granada, C/Fuentenueva s/n, Granada 18071, Spain

ABSTRACT

In order to generate homogeneous magnetophoretic forces, current magnetic tweezer devices operate placing electromagnetic inductors far enough from the sample. Consequently, high-power supplies are needed to reach sufficiently large forces. We demonstrate that both magnetophoretic force magnitude and homogeneity can be increased at will in this kind of devices by simply placing appropriate magnetic materials between the inductors and the sample. Choice of these material shape and location is made upon an extensive optimization process performed with finite element method simulations. Optimal configuration is shown to create large and homogeneous magnetophoretic forces over areas extensive enough to perform multiplexed microrheology tests with different values of force and pulse duration. A good correspondence is obtained between the experiment and the results from the simulations.

1. Introduction

Microrheology encompasses a set of rheometric tools for characterizing the rheological properties of soft materials at a local scale [19]. Typically, a probe is dispersed in the material, whose rheological properties are to be investigated, and its trajectory is measured as a function of time. In passive microrheology the probe moves due to Brownian motion [23,34]. In contrast, in active microrheology the probe motion is imposed by a well-defined external force (optical, magnetic, etc.) what allows motion control and measurement even in complex systems such as biological samples where energy consuming constituents (i.e. living cells) and/or nonequilibrium structures are typical [23,59,33].

Magnetic Tweezers (MTs) belong to the active microrheometry class. They were born in the 50 s for the mechanical characterization of the cytoplasm by combining the knowledge of hydrodynamics and magnetism into one device [49,14]. In a MT, magnetic field generators are used to manipulate magnetic microprobes within a wide range of materials [26]. Two different kinds of magnetic generators are used in the operation of a MT; permanent magnets [49] and active coils (with or without poles) [26,45]. Regarding the materials, they include, among others, cells [47,35,51,42,5], tissues [7,2], biomolecules

[49,54,16,15,28,61,56,39,13,36,43], and colloidal dispersions [26,60]. In a typical application, magnetic microparticles become magnetized under the presence of the external magnetic field and experience a magnetophoretic force that depends on both the magnetic field strength and gradient [8]. Due to this force the magnetic particles move and from their movement the microrheological behavior of the carrier is measured.

Apart from the classical application described above, more recently, further applications involve the use of control algorithms to set a desired position for the probe, by compensating the previously acquired viscosity values of the fluid [25,21]. As a result, MTs can be doubly used either as a force transducer or a positioning system. Both capabilities require a careful description of the magnetic field landscape and a videomicroscopy system with large enough magnification to follow the trajectories of the magnetic microparticles.

If compared with other tweezers, like optical or acoustic, traditionally, MTs exhibit clear advantages. Some of them are as follows: i) they are more independent of the surrounding medium: they can penetrate opaque samples, trap objects with refraction indexes similar to the carrier and even work in vacuum, ii) they do not (photo)damage the samples, iii) they can operate at low frequencies without stability issues exhibited by optical tweezers and iv) in addition to a force, MTs can also

---

Table 1
COV. Comparison of different MT from the literature. *Forces have been normalized to that applied to a magnetic bead of 3.77 μm with independence of their corresponding magnetization.

Size of sample region (μm)	Normalized force* (pN)	COV (%)	Active Dimensions	Citation
75	90	N/A	1D	[43]
60	60	~70	1D	[51]
50	1000	>100	1D	[2]
37.5	0.9	11	1D	[26]
1.5	13.4	~25	1D	[15]
1	210	N/A	1D	[16]
0.4	30	N/A	1D	37
0.015	120	17	1D	[54]
0.015	330	N/A	1D	[62]
0.1	31	1	1D	[61]
0.25	27	10	1D	[64]
15	1.4	>1000	1D	[21]
100 × 100	5.0	>100	2D	[63]
10.000 × 10.000	3.3	N/A	2D	[65]

generate a torque on the sample. In particular, the possibility to generate a torque in the sample is of paramount importance because three additional degrees of independent actuation are added to the system [1]. Moreover, unlike forces, torques do not rely on the magnetic field gradient so it is easier to impose angular velocities to multiple beads simultaneously [26]. This opens the door to microrobotics, e.g. making possible the control of swarms of microrobots by imposing rotation to artificial flagella [14,21,40,58]; directly making them roll as microwheels [44,53,42–45,10,47–52,20,31]; reconfiguring ferrofluids [22–32,17]; or actuating micro mechanisms [24]. microrobot's movement can be assisted using acoustic fields to generate more complex patterns in the microrobot's swarms [3,4].

The capability of MTs for manipulating multiple particles at the same time is known as multiplexing [49]. Undoubtedly, the main advantage of multiplexing is the increased speed of the experiments and their repeatability due to the higher number of microparticles (in a bigger sample volume) which allow to measure statistical distributions. However, the price to pay is a larger distance between the magnetic poles and therefore a smaller magnetophoretic force (see below). Additionally, multiplexing experiments require highly homogeneous magnetophoretic forces (i.e. small variations of magnetic field gradients) on the sample volume, highly diluted samples so that interparticle forces can be neglected and cameras with a wide field of view [26].

Previous publications have usually been oriented towards the generation of homogeneous fields, instead of homogeneous magnetic field gradients. This is so due to the historical focus on the rotating electrical machines, where the magnetic field homogeneity is desired to reduce core losses [11,9]. In addition, high field homogeneity has been also used to detect inhomogeneities in magnetic materials [18]. Halbach cylinders made with permanent magnets [41] or active coils [6] have been a good solution for reaching this objective.

MTs require a homogeneous magnetic field gradient instead of a homogeneous magnetic field strength as they are aiming to exert a force within the sample situated between the generators. The distance of these actuators to the center has to be chosen carefully: if it is large, the system is working as a far-field tweezer. This has the advantages that the magnetic field gradient is similar along a wide region and also it is easier to create a Helmholtz configuration [37], however the exciting power supply must be high to maximize the magnetic field strength. On the other hand, if they are close to the analyzed region, highly inhomogeneous magnetic fields are produced. This effect is produced because the magnetic fields generated by magnetic volumes are homothetic, this means that if we scale the magnetic object maintaining its shape the field lines will enlarge or shrink while maintaining their pattern. As a result of this, by enlarging the magnetic components we can produce higher

values of magnetic intensity $\vec{H}$ However, the field gradient $\nabla\vec{H}$ will be reduced as the magnetic lines need to cover larger distances before reducing its magnitude.

In the current study, we are focusing on the optimization of the magnetic actuators. This will allow to create stronger and more homogeneous forces regardless the used probes. The proposed method to enlarge the magnetic force and its homogeneity is based on the shape, geometry and magnetic properties of magnetic materials inserted in the gap between the magnetic actuators and the sample. As mentioned before, most references in the literature related to the optimization of magnetic actuators are looking for field strength uniformity instead of its gradient uniformity, like [11,9]. In [55], an optimization is performed just aiming to increase the force but not its homogeneity for 1D permanent MT. In the current work two main hypotheses are set: 1.- The implementation of magnetic materials in specific places can increase susbtantially the force applied to the beads. 2.- The force can maintain the same value along the analyzed sample region with that configuration. In addition, by allowing the magnetic materials to be removable, the MT could also work in a far-field mode, providing a more homogeneous field. This interchangeably configuration is useful for applications that aim to produce rotating fields or set a constant magnetization in the beads.

The use of multiplexed MTs is an ideal platform for the realization of microrheological experiments. However, publications so far are limited to small sample volumes (hence reducing the number of microparticles) and the optimization processes solely focus on the maximization of the magnetophoretic force (regardless of the magnetic field gradient homogeneity). In this manuscript, we design, construct and optimize a magnetic field generator that produces homogeneous (theoretical variation around 7% and experimental COV around 30%) and strong (1.1pN) magnetophoretic forces for high precision microrheological applications in an unprecedently large sample region (circle of 800 μm diameter). The device is then tested carrying out microrheological experiments in a MT with carbonyl iron magnetic beads of 3.77 μm with a magnetic contrast factor of 0.65. We use the coefficient of variation (COV) of the magnetophoretic force similarly to [26], defined as the standard deviation divided by the mean of the bead's forces.

In Table 1 we show COV as reported in previous publications in the literature in order to compare with our results. As observed, one common strategy followed to reduce the COV has been to work with reduced workspaces as the gradient's variation is lower as done by [54,61,62,43,13,51,2], where the distance covered was in the nanoscale mostly aiming to handle DNA chains or biomolecules. Other strategy is to increase the separation of the poles to reduce force inhomogeneity, obtaining lower force values [26,42]. In [26], an additional strategy was used based on selecting those particles with similar size to reduce their polydispersity. The MT that considers 2D regions use to have very large workspaces, however no clear indications were found in literature about their force homogeneity [63], Kim (2013). In other cases where isolated bodies are considered in larger working volumes, like in the case of micromanipulators, the movement of the particle can be exerted by closed-loop controllers based on bead's vision trackers to ensure precision Kummer [30], Zhang [57].

Section 1 has set a scope of this research attending to the necessities observed from the state of the art. Section 2 provides a specific theoretical background related the magnetophoretic force. In section 3, the MT is described as well as the optimization process. Section 4 defines the methodology and experiments to test the optimized MTs in microrheology experiments. Finally, section 5 discusses results from simulations and experiments and set the conclusions.

2. Theoretical background

The actuation provided by a MT to a magnetic microparticle is the magnetophoretic force ($\vec{F}$). This force is due to the interaction between
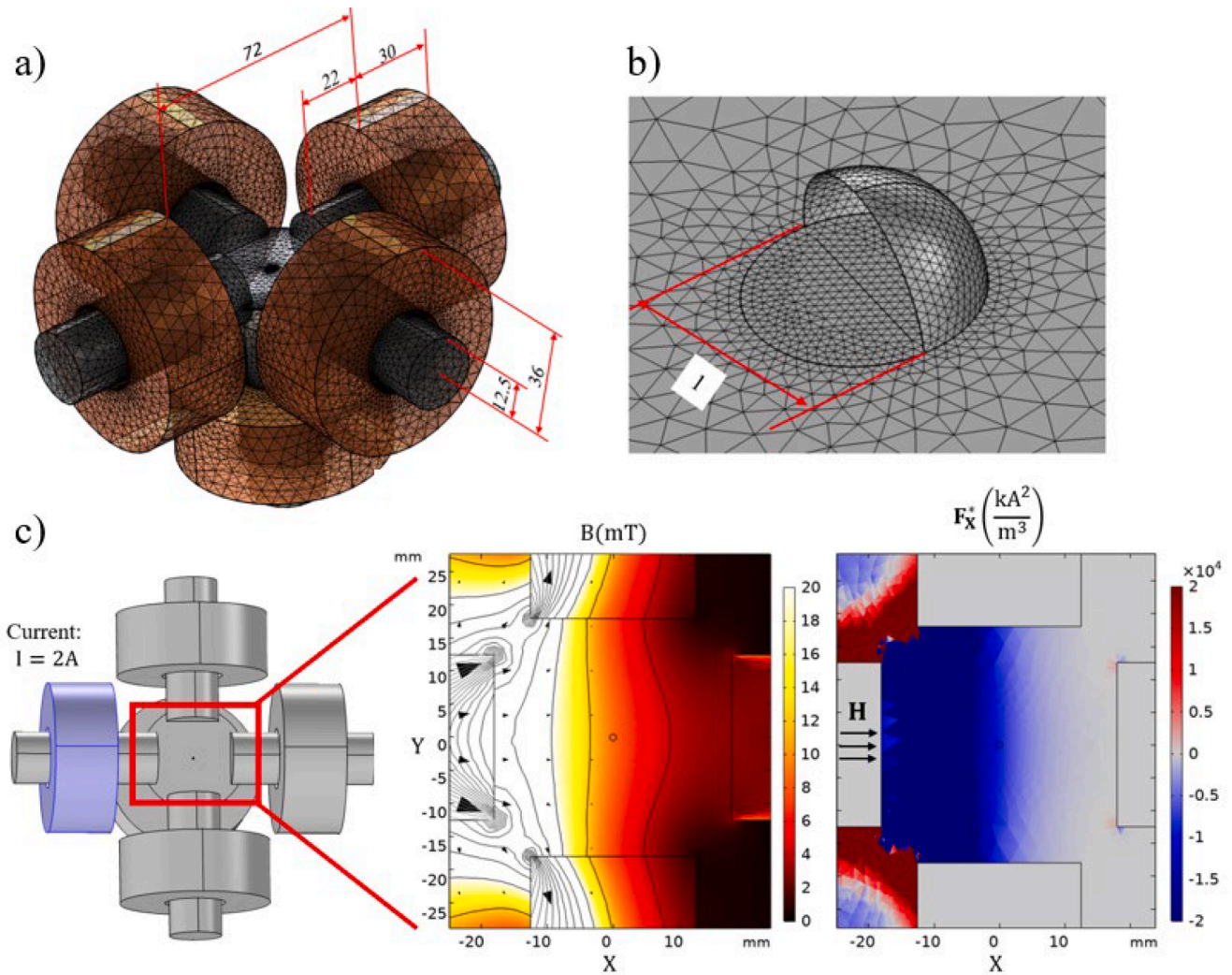
Fig. 1. a) finite element model of the mt consisting of 5 coils. black cylinders represent the mumetal cores. b) sample region where the beads are situated. c) top view of the mt model with the left coil activated with a current of 2 a, magnetic flux density and horizontal component of the magnetophoretic force (F_X^*). The beads feel a force to the left in the blue region, while the force is to the right in red regions. Length scale in mm.

the magnetic field generated by the MT and the magnetized microparticle [27]:

$$\vec{F} = \mu_{cr}(\vec{m} \cdot \nabla)\vec{H} \tag{1}$$

Here μ_{cr} is the magnetic permeability of the medium, $\vec{m}$ is the magnetic moment of the magnetized microparticle and $\vec{H}$ is the external magnetic field generated by the MT.

Under the assumption that the magnetic microparticles are spherical in shape (radius α), their magnetic moment in the linear magnetization approximation (small fields) is given by:

$$\vec{m} = 4\pi a^3 \beta \vec{H} \tag{2}$$

being β the contrast factor between the particles and the carrier.

In view of the fact that Boyer ([12]):

$$\vec{m} \times \left(\nabla \times \vec{H}\right) = 0 \tag{3}$$

Equations (1) and (2) can be combined to get:

$$\vec{F} = 2\pi\mu_{cr}a^3\beta\nabla\|\vec{H}\|^2 \tag{4}$$

being μ_{pr} the particle's magnetic permeability. Once we know the force

acting on the magnetic microparticles, their speed within a linear viscous liquid (viscosity η) can be calculated using the Langevin equation Reenen (2014), [54]. In the case of interest in this work, due to relatively large values that $\vec{F}$ can achieve and the low Reynolds number involved in the application, the velocity of the microparticle ($\vec{V}$) can be computed using the Stokes' law ([26]):

$$\vec{V} = \frac{\vec{F}}{6\pi\eta a} \tag{5}$$

In cartesian coordinates, from Equation (4) the following relationship can be set for a normalized magnetophoretic force:

$$\vec{F^*} := \left[\frac{\partial\|\vec{H}\|^2}{\partial x}, \frac{\partial\|\vec{H}\|^2}{\partial y}, \frac{\partial\|\vec{H}\|^2}{\partial z}\right] \tag{6}$$

Interestingly, for a given set of particles (α and μ_{pr}) and carriers (η and μ_{cr}), the magnetophoretic force is dictated by the gradient of the square of the applied magnetic field.

In this manuscript we fix the sample volume where particles are immersed and pursue two goals. On the one hand, the magnetophoretic force will be maximized. According to Equation (4) this is equivalent to
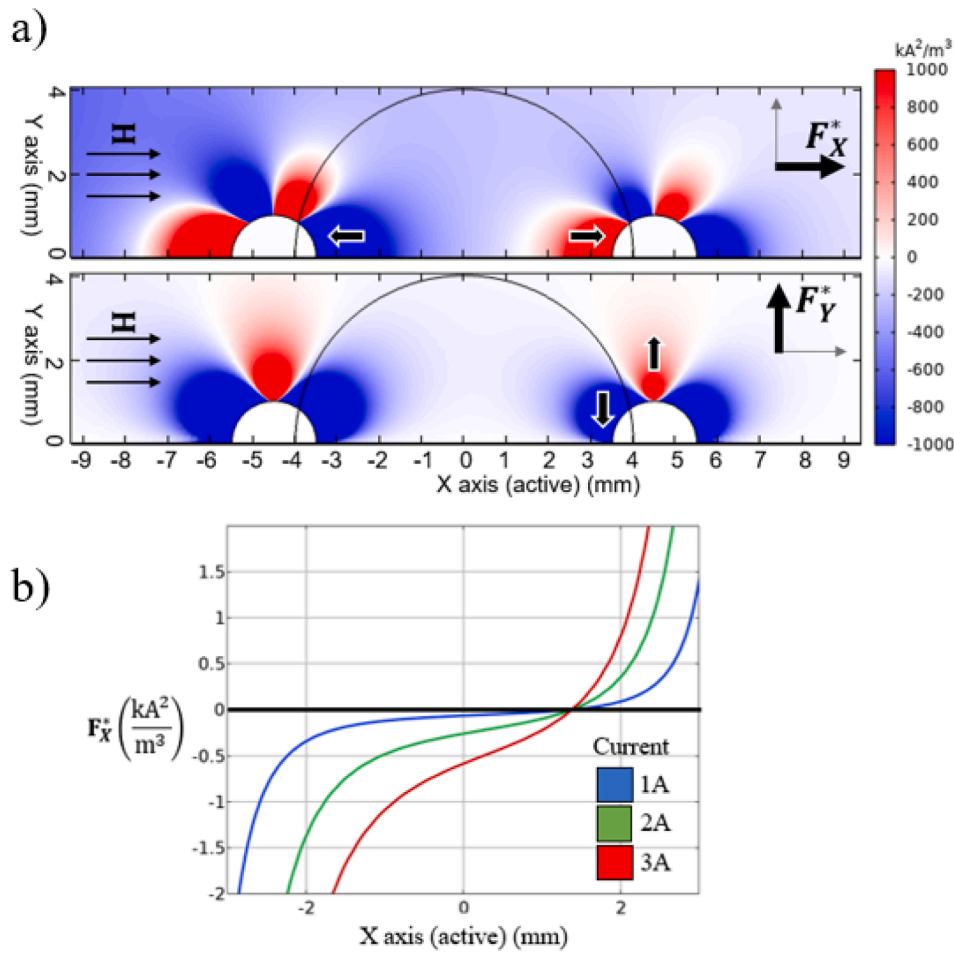
Fig. 2. (a) top view of the center region of the mt when activating the left x coil. Two iron spheres (1 mm radius) are emplaced at both sides of the sample region (4.5 mm apart from the center). The upper panel corresponds to F_x^* (red-right, blue-left) while the lower panel corresponds to F_y^* (red-up, blue-down). b) F_x^* along the x axis for different electric currents circulating along the left x coil.

maximize $\nabla \left\| \vec{H} \right\|^2$ The second goal is to maximize the homogeneity of the magnetophoretic force.

3. Prototype description

We start from a triaxial field generator initially designed and constructed in our laboratory to generate uniform magnetic fields (i.e. negligible field gradients) in a large cylindrical volume (1 cm radius and 1 mm height) for magnetorheological applications [45]. Hence, the magnetophoretic force in this particular setup is negligible. The generator consists of 5 coils of 612 turns of 1 mm² copper wire: One pair aligned with the × axis, other pair aligned with the × axis and one coil for the vertical axis. This configuration allows to have access through the upper aperture to set microscopes, illumination or refrigeration systems, etc.. The windings are symmetrically placed respect to the axes intersection (center of the setup) and are rolled around MuMetal cylindrical cores (Magnetic Shield Corp.) of 68 mm length. Fig. 1a shows the sketch of the setup.

With this device, inhomogeneous magnetic fields can be easily created just energizing one of the windings. In Fig. 1c the magnetic field distribution (predicted by finite element simulations, COMSOL Multiphysics) on the xy plane is shown when a current of 2 A flows through one winding. As can be seen, the magnetic induction lines tend to follow the MuMetal cores and converge in the shaped regions. This generates a gradient that creates a force towards those shaped vertices. In Fig. 1c, this trend in the forces is shown noticing that the magnetic beads will

move towards the active coil except in those regions close to the vertices of the non-active MuMetal cores.

To get a quantitative insight on the induced magnetophoretic force, its magnitude and inhomogeneity are evaluated in a circular region in the center of the MT with diameter of 0.8 mm (later, this will be the area where the experimental sample is analyzed). In this context, the inhomogeneity is defined as the relative difference between the maximum and the minimum values of the magnetophoretic force in the region of analysis. For the case shown in Fig. 1c, we have $\left| F_x^* \right| = 0.9 \cdot 10^4 \pm 6.8\% \left(\frac{kA^2}{m^3} \right)$.

In order to generate a stronger and more homogeneous magnetophoretic force with the triaxial field generator, a possibility consists in inserting a magnetic material in between the poles and the sample. A similar approach has been successfully reported in the literature [26,47]. As a way of example, Fig. 2 shows the simulated magnetophoretic force in the xy plane when only one winding (in the x axis) is active and two magnetic spherical insertions (1 mm radius) are placed along the winding axis (4.5 mm from the setup center). Fig. 2a shows the contour plot of the Cartesian x and y components of the normalized magnetophoretic forcé F_x^* and F_y^* The magnitude of F_x^* ($|F_x^*|$) decreases with the distance to the spherical inserts. As expected, $|F_x^*|$ increases when increasing the current circulating through the active coil (see Fig. 2b) but the price to pay is a much more noticeable force gradient that is not desirable. Note that the non-active y axis also exerts a force which tends to maintain the magnetic microparticles in the center line along the x axis stabilizing the system under perpendicular
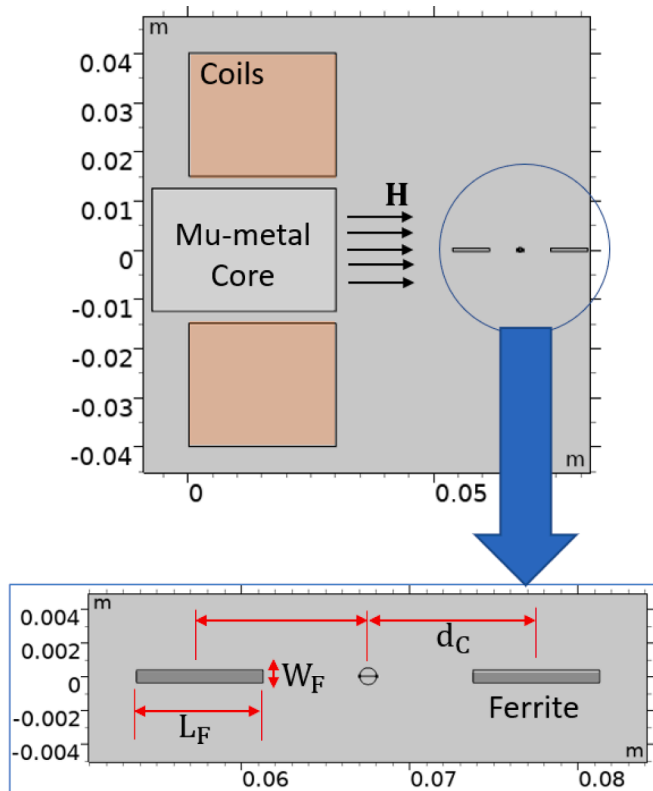
Fig. 3. 2D simulation of the MT with 2 ferrites with 3 configurable parameters for the optimization: The width (W_f), the length (L_f) and the distance from the center of the ferrite to the center of the sample (d_C). The electric current through the coil is 2 A.

Table 2
Force in the active axis as obtained in the sample region for different allowable relative errors. Results are obtained using 2D finite element simulations and optimizing sizes and positions of the ferrites when limiting the maximum relative error allowable. 1000 configurations were evaluated for each restriction. For 2D simulations, the normalized force without ferrites is $|F_x^*| = 46 \pm 4\% \left(\frac{\text{kA}^2}{\text{m}^3}\right)$.

Max. error (%)	L_f(mm)	W_f(mm)	d_C(mm)	$|F_x^*|\left(\frac{\text{kA}^2}{\text{m}^3}\right)$
1	26.5	29.3	18.1	$10 \pm 1\%$
2	29.6	26.7	22.1	$58 \pm 2\%$
3	30.5	19.8	21.2	$115 \pm 3\%$
4	30.1	15.6	19.7	$148 \pm 4\%$

Table 3
Results from 2D simulations of the magnetophoretic forces in the active axis corresponding to commercial ferrites and different distances to the sample.

d_C(mm)	$|F_x^*|\left(\frac{\text{kA}^2}{\text{m}^3}\right)$	
	$W_f = 0.75$ mm; $L_f = 7.5$ mm	$W_f = 3$ mm; $L_f = 25$ mm
6	$225 \pm 107\%$	$749 \pm 40\%$
7	$145 \pm 51\%$	$569 \pm 29\%$
8	$111 \pm 29\%$	$439 \pm 22\%$
10	$81 \pm 14\%$	$309 \pm 15\%$
14	$63 \pm 7\%$	$223 \pm 9\%$
20	$55 \pm 5\%$	$141 \pm 6\%$

perturbations.

To improve not only the magnetophoretic force strength but also its homogeneity within the sample volume we used other insertions. Concretely, we chose ferrite as a material (because of its high magnetic permeability $\mu \cong 2300$, low price and availability in the market) having cylindrical shape (to efficiently guide the flux lines towards the sample).

A schematic of the MT including ferrites along the x axis is shown in Fig. 3. The final ferrite dimensions (width W_f and length L_f) and position (distance to the sample volume d_c) were chosen according to an exhaustive optimization process.

This was performed by running FEA simulations (in 2D or 3D depending on the particular configuration symmetry) of the whole generator with ferrite insertions setting for W_f L_f and d_c random values with uniform distributions (stochastic optimization). In all those simulations Maxwell's equations are solved when only one winding of the x axis is active (current of 2 A) to generate a field gradient. Magnetic behaviors of all MuMetal cores and ferrite insertions were taken into account through the magnetization curves provided by the manufacturers. Rest of domains in the simulation are assumed to have the vacuum permeability, so they are non-magnetic.

The simulated system was encompassed by spherical computation region 10 cm radius and zero flux was applied in its sides/faces as boundary conditions. Regarding the grid, a non-regular non-uniform grid based on second-order tetrahedrons was used. Close to the device center, where field gradients are of interest, the grid has a size in the range of 1 μm and 50 μm while it was coarser, up to 25 mm, in the rest of the computational domain. The most precise analysis region, shown in Fig. 1.b has a maximum grid of 25 μm. Result of this grid, most of the performed simulations have less than 1.5e6 degrees of freedom while the number of elements is between 1 and 2 million. Growing rate of the elements is set to 1.35. The used iterative solver is the FGMRES (flexible generalized minimum residual) with a convergence criterion based on a relative tolerance of 10^{-3} in a maximum number of 100 iterations. Nonlinear resolution is made by a damped Newton's method approach with a relative tolerance of 10^{-3}.

First simulations were performed in the horizontal 2D plane of the ferrites and the magnetic beads, flushing the core face with the coil to increase the range of configurations for the ferrites. As optimum configuration it was chosen the one that maximizes the net force in the active axis (F_x^*) and limits its inhomogeneity below the error of the configuration without any ferrite. Those simplified simulations allow us to analyze multiple ferrite configurations to have a previous idea of the qualitative feasibility of the optimization. For the 2D simulations, normalized force without ferrites and 2 A applied was $|F_x^*| = 46 \pm 4\%$ $\left(\frac{kA^2}{m^3}\right)$ In view of this value, a boundary for the force homogeneity was set to 4 %. Table 2 clearly shows that there exist solutions that increase the force strength keeping its homogeneity below 4 %. However, those values are achievable for very accurate ferrite's sizes difficult to achieve experimentally. The next step was to select commercial ferrites as they are very well characterized so accurate relationship between simulations and actual performance can be established. As observed in Table 3 the force values for commercial ferrites with $W_f = 3$ mm and $L_f = 25$ mm have reasonably small values for homogeneity (but larger than 4 %) for large values of d_c providing similar values to those from non-restricted shape ferrites.

The next step is to incorporate other two ferrites of equal size in the y axis and to run 3D simulations again to ascertain the influence of these ferrites. In Fig. 4, the left coil is again activated with 2 A and a force towards the left appears in the central region. As observed in Fig. 4a, again, as the distance between the ferrites and the sample is reduced, the force is increased and its homogeneity reduced. Magnetic density and force values for these configurations are shown in Table 4. For longer distances between the ferrites and the sample the force still increases with respect the non-optimized case while the homogeneity is just
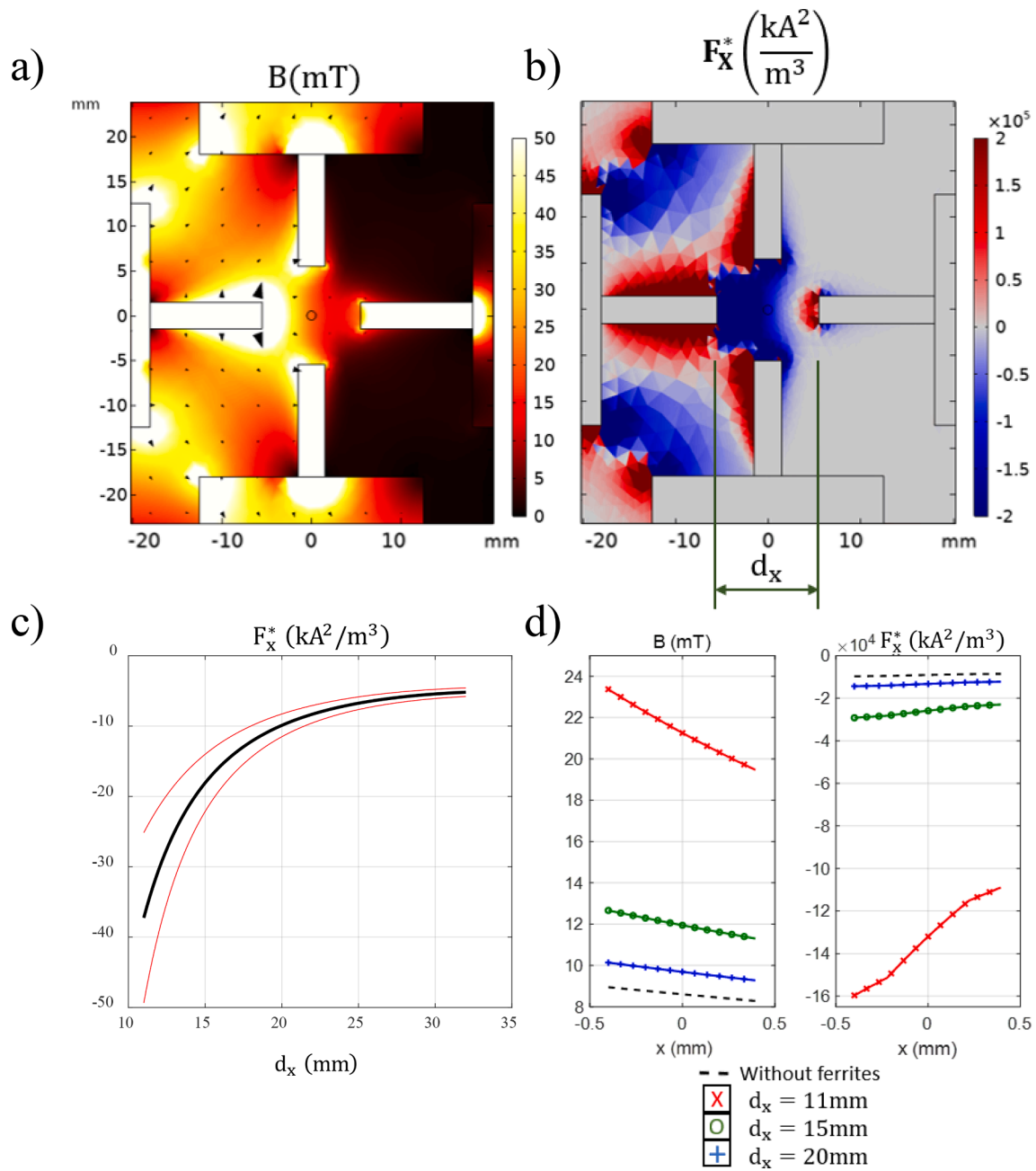
Fig. 4. Commercial ferrites ($W_f = 3$ mm) in a distribution for 2 axes, magnetic field lines and magnetophoretic forces. a) Magnetic flux density. b) Normalized magnetic force along the x axis. Forces that push particles towards the left are in blue while forces that push the particles to the right are in red c) Normalized magnetic force along the xx axis being in black the mean value and in red the boundary values along the workspace and d) Magnetic flux density and normalized magnetophoretic force along the x axis for different separation between the ferrites.

Table 4
Results from 3D simulations of magnetic density and magnetophoretic force for ferrites ($W_f = 3$ mm) arranged in the configuration shown in Fig. 4.

		B_x(mT)	$\lvert F_x^* \rvert \left(10^4 \, \text{kA}^2/\text{m}^3\right)$
No ferrites		$8.6 \pm 3.9\%$	$0.9 \pm 6.8\%$
$d_x = 11$ mm	$L_f = 12.5$ mm	$21.3 \pm 9.7\%$	$13.2 \pm 21.4\%$
$d_x = 15$ mm	$L_f = 10$ mm	$12.0 \pm 5.9\%$	$2.6 \pm 13.6\%$
$d_x = 20$ mm	$L_f = 7$ mm	$9.7 \pm 4.6\%$	$1.3 \pm 9.0\%$

slightly smaller making the $d_c = 20$ mm case an appropriate candidate for the final prototype.

Despite the improvement of the force observed in Table 4, the relative error is higher than in the case without ferrites in all the analyzed cases. To improve this result, four additional ferrites are placed at $+45\,°$ and $-45\,°$. This configuration is shown in Fig. 5. As observed in the simulations, the same trend is found with respect to the distance. Table 5 shows the values corresponding to the configuration represented in Fig. 5. As observed, the configuration $[d_x, d_{xy}] = [15, \, 11]$ *mm* provides very good values with respect to the configuration without ferrites and with respect to the 4 ferrites optimization: The force has been multiplied by 2.8 while the relative force error has been reduced from 6.8 % to 5.9 %. This is the prototype that was built and tested against experiments in the next section.
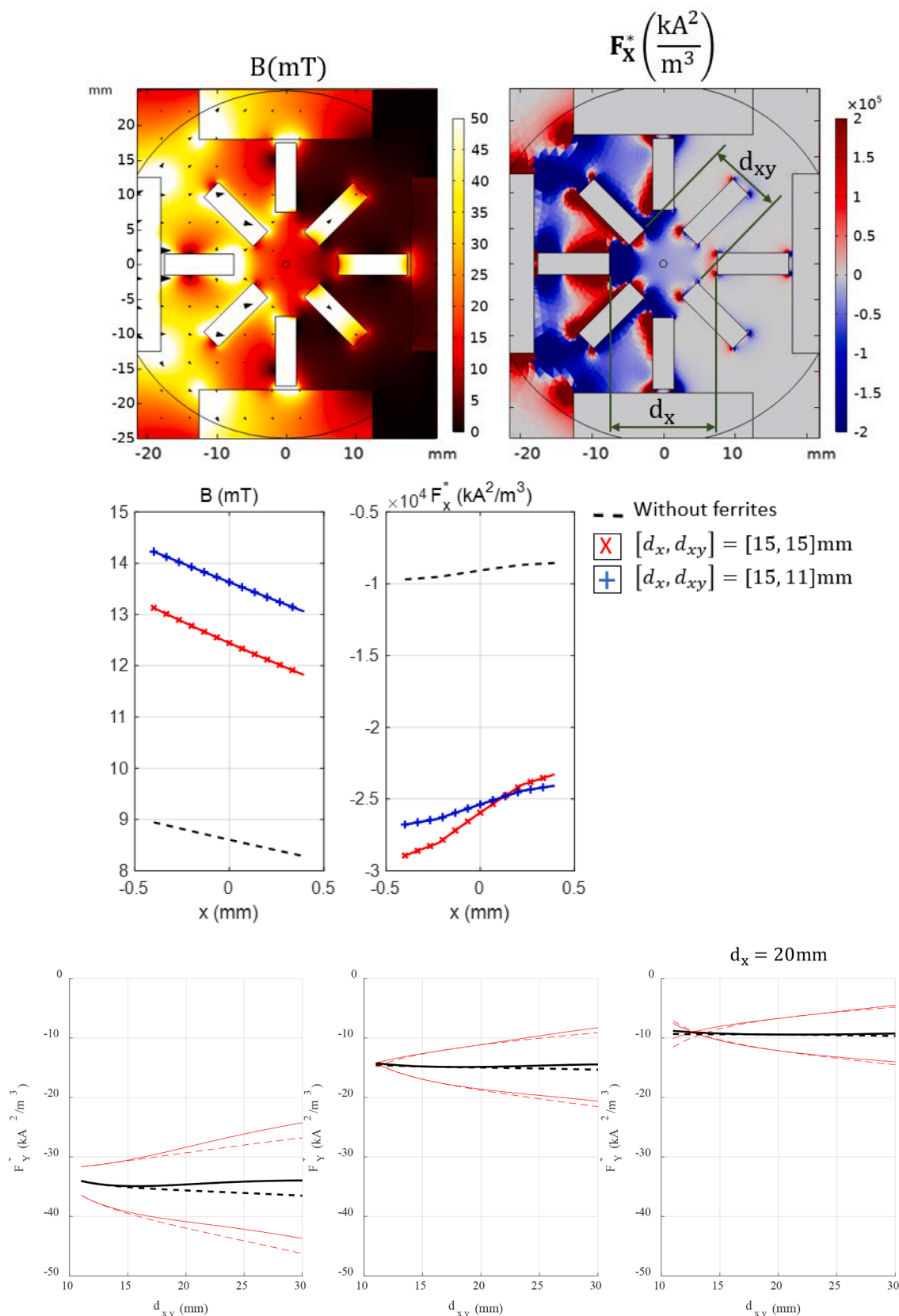
Fig. 5. Commercial ferrites ($W_f = 3$ mm) with a distribution in 4 axes, magnetic field lines and magnetophoretic forces. a) Magnetic flux density and normalized magnetic force along the *x* axis. Forces that push particles towards the left are in blue while forces that push the particles to the right are in red b) Magnetic flux density and normalized magnetophoretic force along the *x* axis for different separation of the ferrites. c) Results from the 2D optimization in the horizontal plane where the ferrites are emplaced. Solid lines correspond to the case where all the ferrites are cut to the same length. Dotted lines correspond to the case where the 45 ° ferrites preserve a length of 15 mm while the others have variable length to have place in the space between the cores.

Table 5

Magnetic field density and magnetophoretic force corresponding to the ferrite configuration shown in Fig. 5 with all the ferrites cut to the same length.

	B_x(mT)	$|F_x^*|\,(10^4\,\text{kA}^2/\text{m}^3)$
No ferrites	$8.6 \pm 3.9\%$	$0.90 \pm 6.8\%$
$[d_x, d_{xy}] = [15, 15]$mm	$12.5 \pm 5.4\%$	$2.5 \pm 12.3\%$
$[d_x, d_{xy}] = [15, 11]$mm	$13.6 \pm 4.4\%$	$2.5 \pm 5.9\%$

## 4. Microrheology experiments

Fig. 6 shows a picture of the MT used in the experiments. Ferrites of width 3 mm and length 10 mm were used. The holder was built in PLA using a 3D printer Ultimaker 3. The ferrites were purchased from Fair-Rite Products Corp. and were simulated assuming a magnetization curve without coercivity. The influence of this magnetic remanence from the ferrites was analyzed by tracking the movement of the magnetic beads after the external field was applied. No significant bead's movement was observed when this external field was removed due to the fact that the magnetophoretic force exerted by this remanence was lower than the friction between the particles and the surface. The ferrites have been cut to their corresponding lengths and attached to the corresponding grooves, serving as a method to ensure that all ferrites have the same length.

The samples used to perform the microrheometry experiments consisted in dilute water suspensions of iron microparticles (grade OM, from BASF SE Germany). These particles are spherical in shape with a 3.77 μm diameter and $\beta = 0.65$. Prior to the experiment, a drop of the suspension was kindly placed on top of a glass slide of 0.15 μm thickness. Then, the suspension was allowed to rest for the particles to sediment.

The microrheometry test consisted in activating the two coils of the × axis alternatively during different intervals of time (0.5, 1, 1.5 and 2 s) and different currents (1, 1.5, 2 and 2.5 A) (see Fig. 7). These experiments were repeated without and with ferrites in the optimal configuration. The periodic movement of the magnetic microparticles was recorded with a high-speed camera (Photron MiniAX) at 20 fps with 1/1000 s aperture time and 512×512 pixels resolution. Images were analyzed using a custom-built Matlab code. Several filters were used. Firstly, a low pass filter (F#1) (Butterworth of 4 order) at 4.5 Hz was used to remove noise produced by the MTs vibration. Filters were also necessary to remove movements with a duration shorter than 75 % of the duration of the magnetic pulse (F#2), with a displacement smaller than half a pixel (0.87 μm) (F#3), movements leaving the region of analysis (a circle in the xy plane of diameter 800 μm) and also the outliers, defined as those particles whose displacement is bigger than 2 times the standard deviation of the displacement of all the beads considered (F#4). Those outliers filtered with F#4 use to be due to interactions between particles as they use to show few cases of higher
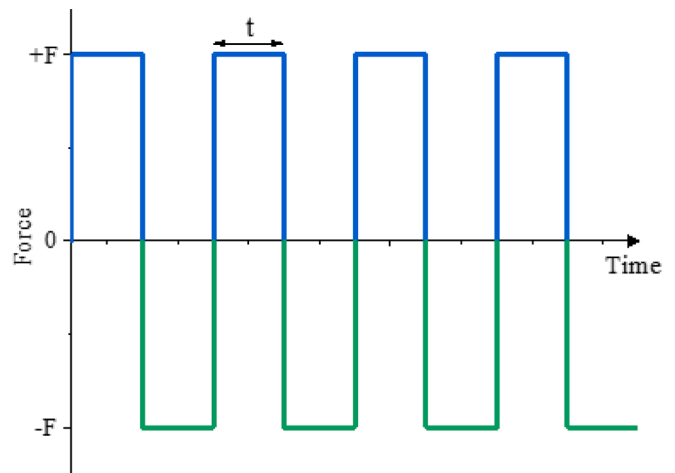
Fig. 7. Schematics of the microrheometry experimental protocol. The two coils are fed alternatively to produce forces (*F*) in opposite directions. Different pulse durations (*t*) are tested, ranging from 0.5 s to 2 s.
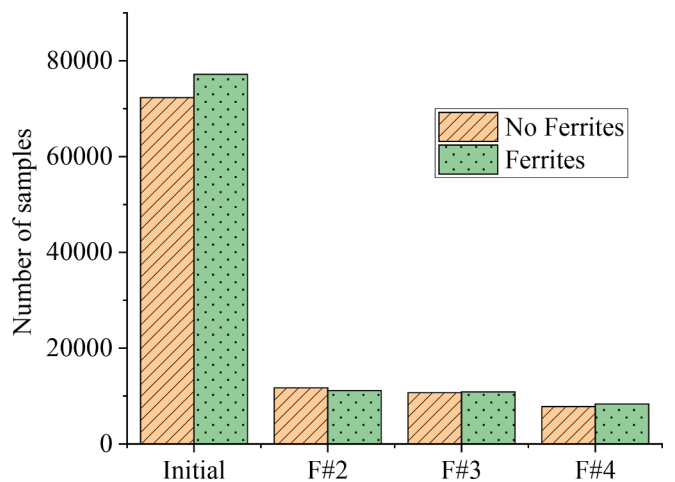
Fig. 8. Number of samples remaining after applying each filter for the 32 tests (2 tests for each pulse condition). F#1: low-pass filter. It does not discard any sample as it just reduces high frequency vibrations. F#2: timing filter, F#3: minimum displacement filter, F#4: inside analysis region.
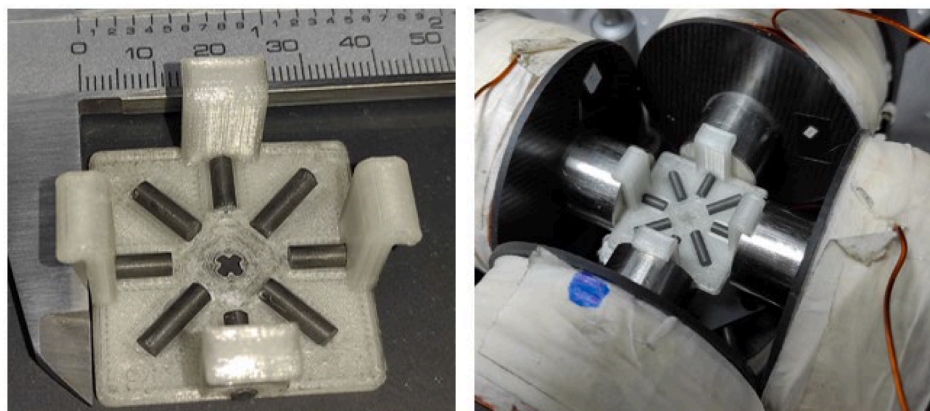
Fig. 6. a) Removable prototype with the ferrites distribution in a 3D printed PLA support. b) Prototype attached to the actual MT to optimize its performance.
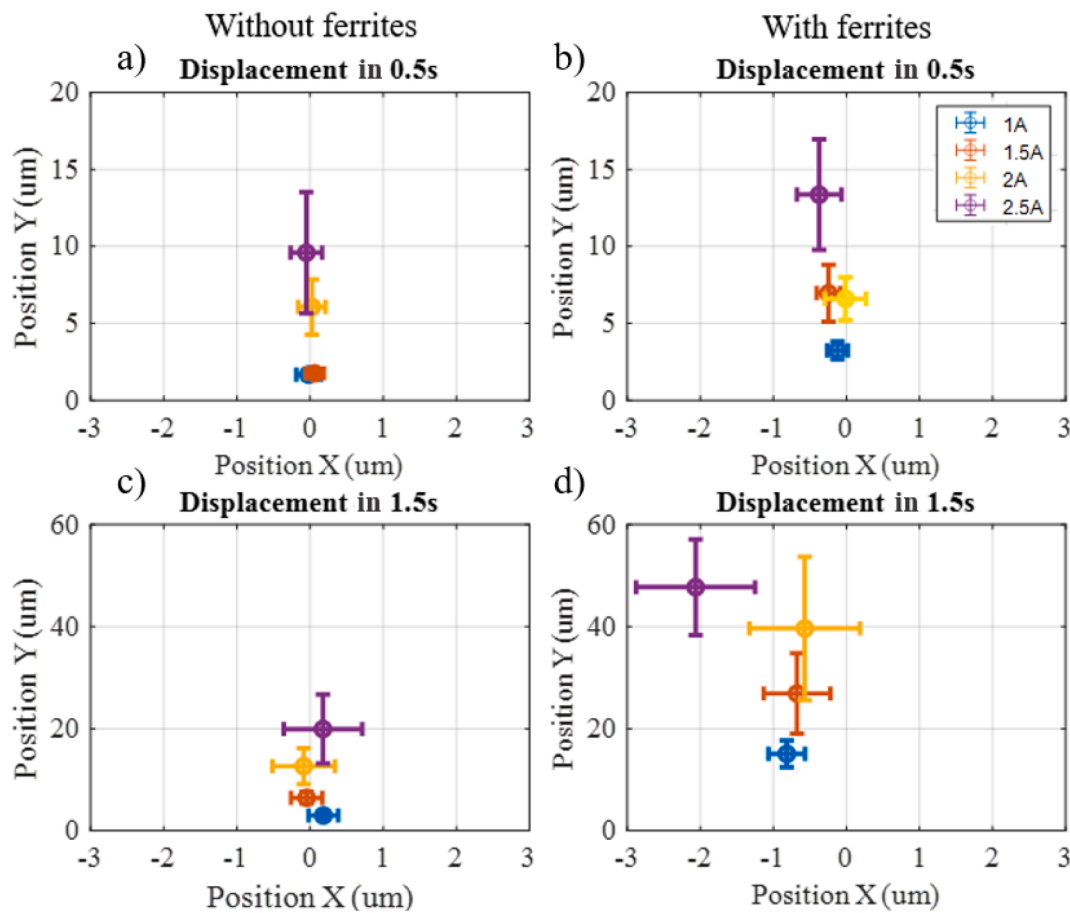
Fig. 9. Final displacement of the beads for pulses of 0.5 s and 1.5 s for currents of 1, 1.5, 2 and 2.5 A. Values represented correspond to the mean and standard deviation for the samples considered for each test. a,c) Values corresponding to the magnetic tweezer without ferrites. b,d) Values corresponding to the MT with the ferrite distribution.

Table 6

Theoretical and measured force of the MT before and after the optimization for magnetic beads grade OM, (BASF SE Germany) of 3.77 μm and pulses of duration of 0.5, 1, 1.5 and 2 s. The Reynolds number in these experiments is typically of the order of $10^{-4} \ll 1$. Experimental errors are analyzed in Appendix A.

Prototype	Current	Type	Force (pN)	COV	Samples
No ferrites	1 A	Simulated	0.08 ± 7.36 %		
		Experimental	0.10 ± 93.0%	28.4 %	757
	1.5 A	Simulated	0.18 ± 7.31 %		
		Experimental	0.24 ± 95.8%	37.0 %	1011
	2 A	Simulated	0.31 ± 6.80 %		
		Experimental	0.41 ± 114%	38.9 %	685
	2.5 A	Simulated	0.50 ± 7.59 %		
		Experimental	0.58 ± 108%	36.0 %	881
	1 A	Simulated	0.22 ± 6.55 %		
		Experimental	0.23 ± 69.6%	26.3 %	1410
	1.5 A	Simulated	0.49 ± 6.54 %		
		Experimental	0.62 ± 133%	30.1 %	867
Ferrites	2 A	Simulated	0.87 ± 5.9 %		
		Experimental	0.83 ± 126%	36.8 %	1434
	2.5 A	Simulated	1.35 ± 6.44 %		
		Experimental	1.11 ± 99.1%	21.7 %	845

force values. The efficiency of the filters is demonstrated in Fig. 8. Here we show how the number of microparticles reduces as the filtering proceeds. Note that a large amount of particles were stuck on the glass plate.

The comparison between averaged microparticle displacements for different values of current and illustrative elapsed times are shown in

Fig. 9. It is observed that displacements are lower than the microparticle diameter along the non-active axis. However, along the active axis, the displacement is larger with than without them (compare Fig. 9a and Fig. 9b). In addition, the larger the current or the elapsed time, the larger the displacement (compare Fig. 9a and Fig. 9c). Note that the dispersion of the results is larger for the largest currents and elapsed times.

Using equation (6) and knowing the velocities of the microparticles it is possible to compute the magnetophoretic force and to compare it with the simulations. Results are shown in Table 6 and Fig. 10. A very good agreement is found between the simulations and experiments in both cases, with and without ferrites. As expected, magnetophoretic forces without ferrites (0.41 pN at 2 A) are clearly below the data with ferrites (0.83 pN at 2 A). Despite of the fact that the relative error for the ferrite is higher than the predicted one, the values are equivalent to the prototype without ferrites (38.9 % without ferrites vs 36.8 % with ferrites for 2 A applied). The discrepancy between the predicted error and the measured one can be due to several reasons: local magnetic forces, polydispersity of the beads, agglomeration of particles, etc. To reduce those effects, each test where performed with a newly prepared sample.

Let us now discuss the homogeneity of the magnetophoretic force. In the simulations, the homogeneity has been computed along the central active line. Due to the symmetry of the device, the central line within the active region is where higher relative error is expected. As observed in Fig. 10, relative errors in experiments are larger than simulations. However, this increased variability of the force could be not only due to the inhomogeneous gradient but to other factors such as the interaction between nearby particles, the movement of two or more beads stuck together forming a cluster, etc. An appropriate way to check the
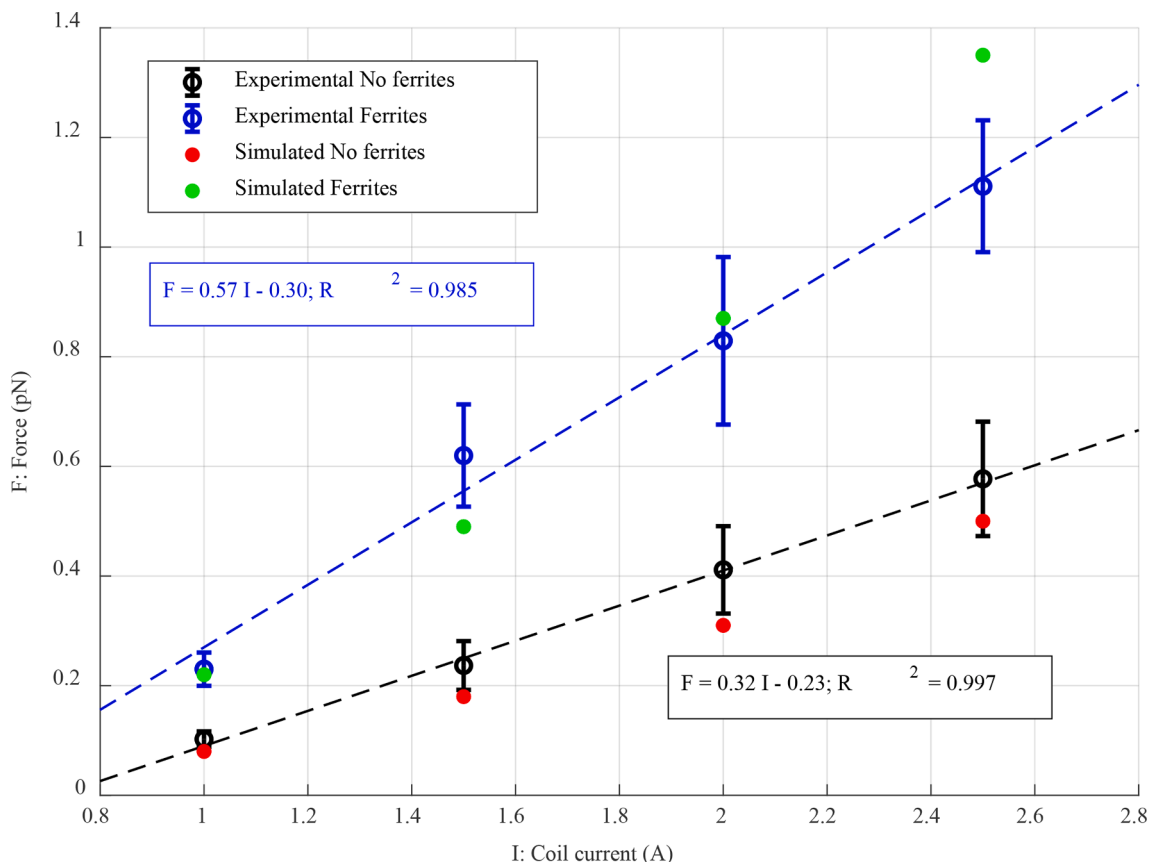
Fig. 10. Magnetophoretic force of the particles for each current applied. Pulsed durations of 0.5 s, 1 s, 1.5 s, and 2 s are applied for each experimental dataset. Adjust curve is set following experimental data from the non-optimized and optimized systems. Simulated mean values are shown as red dots (non-optimized system) and green dots (optimized system).
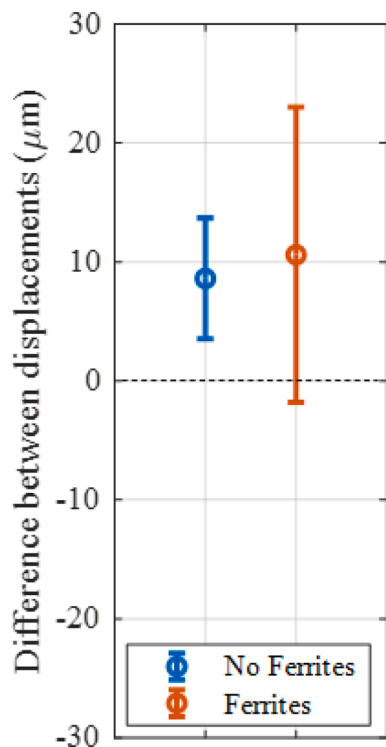

Fig. 11. Difference of the displacements between the particles situated in the region closer to the coil and the region furthest to the coil. Each of these regions are the 25 % of the total area of the analyzed sample.

Table A1

Uncertainty corresponding to the experimental results for each current applied. Different pulse duration experiments have been merged to analyze the robustness of the measure under different duration of the trajectories.

Position uncertainty for pulse duration of 0.5, 1, 1.5 and 2 s				
	Current	Std. dev. (µm)	uA (µm)	uC (µm)
No ferrites	1 A	1.6	0.058	0.066
	1.5 A	5.0	0.16	0.16
	2 A	8.6	0.33	0.33
	2.5 A	13	0.44	0.44
Ferrites	1 A	4.3	0.11	0.11
	1.5 A	17	0.58	0.58
	2 A	28	0.74	0.74
	2.5 A	23	0.79	0.79

Table A2

Uncertainty for the velocity and force corresponding to the experimental results for each current applied. Different pulse duration experiments have been merged to analyze the robustness of the measure under different duration of the trajectories.

Velocity and force uncertainty for pulse duration of 0.5, 1, 1.5 and 2 s			
	Current	$u_C(v)$ [µm/s]	$u_C(F)$ [pN]
No ferrites	1 A	1.3	0.093
	1.5 A	3.2	0.23
	2 A	6.6	0.47
	2.5 A	8.8	0.63
Ferrites	1 A	2.2	0.16
	1.5 A	11.6	0.83
	2 A	14.8	1.1
	2.5 A	15.8	1.1

homogeneity of the applied force within the analyzed sample is to compare the displacement of the particles between the further and closer regions of the workspace. One of them is in the region closer to the active coil while the other is in the opposite region and both have the same surface. The displacements of the particles contained in those regions were tracked for all the currents and pulse durations and the difference between the two regions computed. Fig. 11 shows the results, where the difference of displacements in the direction of the active axis in both regions have a mean value practically equal of 10 μm (around three times the particle diameter). This shows that there is a good force homogeneity in the analyzed area and that the source of variability of the measured force is not due exclusively to the exerted force field.

5. Conclusions

Traditionally, MTs maximize the magnetophoretic force strength without paying attention to the magnetophoretic force homogeneity. This is so because the sample volume is typically small and therefore inhomogeneity is not an issue. However, for sufficiently large sample volumes, such as those needed in multiplexing applications, an appropriate design must take into account both strength and homogeneity.

In this manuscript we show, using finite element simulations and experiments, that it is feasible to enhance both the strength and homogeneity using magnetic inserts in between the sample and the poles by appropriately choosing the ferrites and geometry. At first, we demonstrated that the force homogeneity can be tuned with the length and width of the ferrites. As shown in Table 2, shorter and wider ferrites produce more homogeneous force at the cost of reducing its strength. We have also observed a direct correlation between magnetic force homogeneity and distance between commercial ferrites, obtaining higher forces when they are close to the sample.

The final ferrite configuration, shown in Fig. 5 and Fig. 6, enhances the effect from the basic configuration of two ferrites. The magnetophoretic force is increased by a theoretical factor of 2.5, from 0.31 to 0.87 pN (considering CIP of 3.77 μm) and experimentally by 2.0, from 0.41 to 0.83 pN with the same magnetic beads. However, the measured force does not consider friction and proximity effects that could be proportional to the velocity. The COV (quotient between the standard deviation and the mean) of the experimental data from the case without ferrites is 38.9 % while in the case of the ferrites is 36.8 % for a current of 2 A, slightly lower than without the optimization, as expected. In addition, the applied force was maintained along the analysis region in the sample, providing a homogeneous vector field for the magnetophoretic force with a mean difference of displacement between the closest and furthest region of 10 μm, while displacements with ferrites

use to be larger than this value for adequate values of current and time as shown in Fig. 9. This shows that an important source of errors can come from interparticle interactions, chain formation and heterogeneities in friction and viscosity levels.

Some direct applications of these results are the possibility to exert higher forces with constant values along a wide region to magnetic particles. So this, smaller beads can be used and dispersed over a wider area to provide more accurate microrheology measures, with higher spatial resolution and covering larger samples.

Some possible future lines could point to perform force optimizations considering different materials or shapes and also tridimensional configurations. Results obtained from microrheology experiments proposed could enhance position control of microrobots as a precise viscosity map of the environment could be generated.

CRediT authorship contribution statement

Alejandro Rodriguez-Barroso: Conceptualization, Methodology, Software, Investigation, Validation, Writing – original draft. **Guillermo Camacho:** Conceptualization, Software, Investigation, Validation, Writing – review & editing. **Oscar Martinez-Cano:** Software, Resources. **Jose Rafael Morillas:** Methodology, Writing – review & editing. **Juan de Vicente:** Conceptualization, Methodology, Resources, Writing – review & editing, Supervision, Project administration, Funding acquisition.

Declaration of Competing Interest

The authors declare that they have no known competing financial interests or personal relationships that could have appeared to influence the work reported in this paper.

Data availability

Data will be made available on request.

Acknowledgements

Appendix

The quality of the performed measurements is provided following to the Guide to the expression of uncertainty in measurement (GUM) JCGM: Guides in Metrology. According to the 20 fps used, the time resolution of the videomicroscopy measurement is 0.05 ms. Assuming a uniform distribution of this measurement, the related type B uncertainty is:

$$u_B(t) = \frac{0.05\,\text{ms}}{\sqrt{12}} = 0.014\,\text{ms}$$

While the spatial uncertainty is based on the camera's signal-to-noise ratio (SNR) [38]. This can be deduced from the specifications of the CCD sensor, which has a quantum efficiency (Q_e) of 46% and a size of 20.48 mm × 20.48 mm, working at 25 °C with the illumination source BHDS-00 from Infaimon which provides more than 3000 lx at 15 mm, an integrating time of 1 ms. Scientific grade CCDs use to have values of dark current (I_D) lower than 5 electrons /(s·pixel), and N_r around 10 electrons / pixel, which is a typical value at the working temperature. According to those values, the SNR in similar conditions is provided by [46] for a 1.4 Megapixels camera as SNR = 90.

For a magnetic bead size (a) of 3.77 μm, a pixel resolution (l_n) of 1.74 μm and a mask diameter (m) of 9 pixels, the position uncertainty is given by [38]:

$$u_B(x) = \frac{l_n}{SNR\,2\pi^{\frac{1}{2}}}\frac{m^2}{a^2} = 0.031\,\mu m$$

As observed, type B uncertainty is very reduced in comparison with type A uncertainty, showing that the sensibility of the instruments used is appropriate for the experiments performed. The uncertainty of the velocity has been obtained as indirect measurement with the following expressions:

$$u_C(v) = \sqrt{\frac{1}{t^2}u_C^2(x) + \frac{x^2}{t^4}u_C(t)}$$

The biggest uncertainty values for the velocity are obtained for the minimum sample time, which is $t_{min} = 50$ ms and maximum displacement in that time, which is obtained from Fig. 9, is related to the current applied, having maximum boundary values of 0.67, 1.33, 1.67 and 2 μm for the cases of 0.5, 1, 2 and 2.5 A respectively. The uncertainty in the velocity is chosen for the most unfavorable case (see Table A1).

The uncertainty for the force is obtained from (5) as:

$$u_C(F) = \sqrt{(6\pi\eta a)^2 u_C^2(v) + (6\pi a v)^2 u_B^2(\eta)}$$

Which is solved assuming a sample's temperature of $T = 20 \pm 1$ °C when the experiment was performed, the water's viscosity is $\eta = 1.002 \pm 0.025$ mPa/s, maximum velocity, maximum current, and a constant diameter for the beads of 3.77 μm. Uncertainties for the velocity and force are shown in Table A2. The relative error corresponding to this uncertainty is shown in Table 6.

References

[1] J.J. Abbott, E. Diller, A.J. Petruska, Magnetic methods in robotics, Ann. Rev. Control Robot. Autonomous Syst. 3 (2020) 57–90.

[2] C. Aermes, A. Hayn, T. Fischer, C.T. Mierke, Environmentally controlled magnetic nano-tweezer for living cells and extracellular matrices, Sci. Rep. 10 (1) (2020) 1–16.

[3] D. Ahmed, T. Baasch, N. Blondel, N. Läubli, J. Dual, B.J. Nelson, Neutrophil-inspired propulsion in a combined acoustic and magnetic field, Nat. Commun. 8 (1) (2017) 770, https://doi.org/10.1038/s41467-017-00845-5.

[4] D. Ahmed, A. Sukhov, D. Hauri, D. Rodrigue, G. Maranta, J. Harting, B.J. Nelson, Bioinspired acousto-magnetic microswarm robots with upstream motility, Nat. Mach. Intell. 3 (2) (2021) 116–124, https://doi.org/10.1038/s42256-020-00275-x.

[5] M.B. Akolpoglu, Y. Alapan, N.O. Dogan, S.F. Baltaci, O. Yasa, G. Aybar Tural, M. Sitti, Magnetically steerable bacterial microrobots moving in 3D biological matrices for stimuli-responsive cargo delivery, Sci. Adv. 8 (28) (2022) eabo6163.

[6] N. Alatawneh, P. Pillay, Design of a novel test fixture to measure rotational core losses in machine laminations, IEEE Trans. Ind. Appl. 48 (5) (2012) 1467–1477, https://doi.org/10.1109/TIA.2012.2209849.

[7] D.O. Asgeirsson, M.G. Christiansen, T. Valentin, L. Somm, N. Mirkhani, A.H. Nami, S. Schuerle, 3D magnetically controlled spatiotemporal probing and actuation of collagen networks from a single cell perspective, Lab Chip 21 (20) (2021) 3850–3862.

[8] A.O. Ayansiji, A.V. Dighe, A.A. Linninger, M.R. Singh, Constitutive relationship and governing physical properties for magnetophoresis, Proc. Natl. Acad. Sci. 117 (48) (2020) 30208–30214.

[9] J.B. Bartolo, P. Klimczyk, K. Tiwisina, P. Denke, S. Siebert, C. Gerada, An investigation into the geometric parameters affecting field uniformity in four pole magnetisers, Int. J. Appl. Electromagn. Mech. 48 (2–3) (2015) 225–232.

[10] [JCGM: Guides in Metrology]: www.bipm.org/en/committees/jc/jcgm/publications.

[11] O. Bottauscio, M. Chiampi, F. Fiorillo, A. Manzin, Space and time distribution of magnetic field in 2D magnetizers. In 8th International Workshop on One-and Two-Dimensional Magnetic Measurement and TestIng, 2005.

[12] T.H. Boyer, The force on a magnetic dipole, Am. J. Phys 56 (8) (1988) 688–692.

[13] H.K. Choi, H.G. Kim, M.J. Shon, T.Y. Yoon, High-resolution single-molecule magnetic tweezers, Annu. Rev. Biochem 91 (2022) 33–59.

[14] F.H. Crick, the physical properties of cytoplasm. A study by means of the magnetic particle method. Part II. Theoretical treatment, Exp. Cell Res. 1 (4) (1950) 505–533.

[15] M. Cristofalo, C.A. Marrano, D. Salerno, R. Corti, V. Cassina, A. Mammola, F. Mantegazza, Cooperative effects on the compaction of DNA fragments by the nucleoid protein H-NS and the crowding agent PEG probed by magnetic tweezers, Biochimica et Biophysica Acta (BBA)-General Subjects 1864 (12) (2020) 129725.

[16] P. Daldrop, H. Brutzer, A. Huhle, D.J. Kauert, R. Seidel, Extending the range for force calibration in magnetic tweezers, Biophys. J . 108 (10) (2015) 2550–2561.

[17] X. Fan, Y. Jiang, M. Li, Y. Zhang, C. Tian, L. Mao, M. Sitti, Scale-reconfigurable miniature ferrofluidic robots for negotiating sharply variable spaces, Sci. Adv. 8 (37) (2022).

[18] K. Fukuoka, S. Noma, M. Kobayashi, T. Ozaki, Y. Oikawa, Consideration of multi-coil type magnetizer for detection of omnidirectional crack in magnetic particle testing, Int. J. Appl. Electromagn. Mech. 52 (3–4) (2016) 1537–1543, https://doi.org/10.3233/JAE-162174.

[19] E.M. Furst, T.M. Squires, Microrheology, Oxford University Press, 2017.

[20] G. Gardi, S. Ceron, W. Wang, K. Petersen, M. Sitti, Microrobot collectives with reconfigurable morphologies, behaviors, and functions, Nat. Commun. 13 (1) (2022) 2239.

[21] C. Gosse, V. Croquette, Magnetic tweezers: micromanipulation and force measurement at the molecular level, Biophys. J . 82 (6) (2002) 3314–3329, https://doi.org/10.1016/S0006-3495(02)75672-5.

[22] S.R. Goudu, H. Kim, X. Hu, B. Lim, K. Kim, S.R. Torati, C. Kim, Mattertronics for programmable manipulation and multiplex storage of pseudo-diamagnetic holes and label-free cells, Nat. Commun. 12 (1) (2021) 3024.

[23] M. Guo, A.J. Ehrlicher, M.H. Jensen, M. Renz, J.R. Moore, R.D. Goldman, D. A. Weitz, Probing the stochastic, motor-driven properties of the cytoplasm using force spectrum microscopy, Cell 158 (4) (2014) 822–832.

[24] C. Hong, Z. Ren, C. Wang, M. Li, Y. Wu, D. Tang, M. Sitti, Magnetically actuated gearbox for the wireless control of millimeter-scale robots, Sci. Rob. 7 (69) (2022).

[25] C. Huang, T. Xu, J. Liu, L. Manamanchaiyaporn, X. Wu, Visual servoing of miniature magnetic film swimming robots for 3-D arbitrary path following, IEEE Rob. Autom. Lett. 4 (4) (2019) 4185–4191.

[26] K.C. Johnson, E. Clemmens, H. Mahmoud, R. Kirkpatrick, J.C. Vizcarra, W. E. Thomas, A multiplexed magnetic tweezer with precision particle tracking and bi-directional force control, J. Biol. Eng. 11 (1) (2017) 1–13.

[27] T. Jones Electromechanics of Particles 1995 Cambridge University Press Cambridge 10.1017/CBO9780511574498.

[28] D. Kilinc, G.U. Lee, Advances in magnetic tweezers for single molecule and cell biophysics, Integr. Biol. 6 (1) (2014) 27–34.

[29] M.D. Krebs, R.M. Erb, B.B. Yellen, B. Samanta, A. Bajaj, V.M. Rotello, E. Alsberg, Formation of ordered cellular structures in suspension via label-free negative magnetophoresis, Nano Lett. 9 (5) (2009) 1812–1817.

[30] M.P. Kummer, J.J. Abbott, B.E. Kratochvil, R. Borer, A. Sengul, B.J. Nelson, OctoMag: an electromagnetic system for 5-DOF wireless micromanipulation, IEEE Trans. Rob. 26 (6) (2010) 1006–1017.

[31] Y.W. Lee, J.K. Kim, U. Bozuyuk, N.O. Dogan, M.T.A. Khan, A. Shiva, M. Sitti, Multifunctional 3D-printed pollen grain-inspired hydrogel microrobots for on-demand anchoring and cargo delivery, Adv. Mater. 35 (10) (2023).

[32] S.S. Leong, Z. Ahmad, S.C. Low, J. Camacho, J. Faraudo, J. Lim, Unified view of magnetic nanoparticle separation under magnetophoresis, Langmuir 36 (28) (2020) 8033–8055.

[33] W. Liu, C. Wu, Rheological study of soft matters: a review of microrheology and microrheometers, Macromol. Chem. Phys. 219 (3) (2018) 1700307.

[34] C. Martinez-Torres, A. Arneodo, L. Streppa, P. Argoul, F. Argoul, Passive microrheology of soft materials with atomic force microscopy: a wavelet-based spectral analysis, Appl. Phys. Lett. 108 (3) (2016), 034102.

[35] K. Norregaard, R. Metzler, C.M. Ritter, K. Berg-Sørensen, L.B. Oddershede, Manipulation and motion of organelles and single molecules in living cells, Chem. Rev. 117 (5) (2017) 4342–4375.

[36] Y. Pei, T. Bian, Y. Liu, Y. Liu, Y. Xie, J. Song, Single-molecule resettable DNA computing via magnetic tweezers, Nano Lett. 22 (7) (2022) 3003–3010.

[37] Restrepo, A. F., Franco, E., Cadavid, H., & Pinedo, C. R. (2017, December). A comparative study of the magnetic field homogeneity for circular, square and equilateral triangular helmholtz coils. In 2017 International Conference on Electrical, Electronics, Communication, Computer, and Optimization Techniques (ICEECCOT) (pp. 13-20). IEEE.

[38] T. Savin, P.S. Doyle, Static and dynamic errors in particle tracking microrheology, Biophys. J . 88 (1) (2005) 623–638.

[39] S. Schuerle, I.A. Vizcarra, J. Moeller, M.S. Sakar, B. Özkale, A.M. Lindo, B. J. Nelson, Robotically controlled micorprey to resolve initial attack modes preceding phagocytosis, Sci. Rob. 2 (2) (2017).

[40] A. Servant, F. Qiu, M. Mazza, K. Kostarelos, B.J. Nelson, Controlled in vivo swimming of a swarm of bacteria-like microrobotic flagella, Adv. Mater. 27 (19) (2015) 2981–2988, https://doi.org/10.1002/adma.201404444.

[41] T. Shi, Z. Qiao, C. Xia, H. Li, Z. Song, Modeling, analyzing, and parameter design of the magnetic field of a segmented halbach cylinder, IEEE Trans. Magn. 48 (5) (2011) 1890–1898.

[42] X. Tang, X. Liu, P. Li, D. Liu, M. Kojima, Q. Huang, T. Arai, Efficient single-cell mechanical measurement by integrating a cell arraying microfluidic device with magnetic tweezer, IEEE Rob. Autom. Lett. 6 (2) (2021) 2978–2984.

[43] R. Tapia-Rojo, E.C. Eckels, J.M. Fernández, Ephemeral states in protein folding under force captured with a magnetic tweezers design, Proc. Natl. Acad. Sci. 116 (16) (2019) 7873–7878.

[44] T.O. Tasci, P.S. Herson, K.B. Neeves, D.W.M. Marr, Surface-enabled propulsion and control of colloidal microwheels, Nat. Commun. 7 (1) (2016) 10225, https://doi.org/10.1038/ncomms10225.

[45] M. Terkel, J. de Vicente, Magnetorheology of exotic magnetic mesostructures generated under triaxial unsteady magnetic fields, Smart Mater. Struct. 30 (1) (2021), 014005.

[46] Thorlabs. Camera Noise and Temperature Tutorial. URL: www.thorlabs.com/newgrouppage9.cfm?objectgroup_id=10773.

[47] J.V. Timonen, B.A. Grzybowski, Tweezing of magnetic and Non-Magnetic objects with magnetic fields, Adv. Mater. 29 (18) (2017) 1603516.

[48] A. van Reenen, Y. Gao, A.M. de Jong, M.A. Hulsen, J.M.J. den Toonder, M.W.J. Prins, Dynamics of magnetic particles near a surface: model and experiments on field-induced disaggregation, Phys. Rev. E 89 (4) (2014), 042306.

[49] I. Vlaminck, C. Dekker, Recent advances in magnetic tweezers, Annu. Rev. Biophys. 41 (2012) 453–472, https://doi.org/10.1146/annurev-biophys-122311-100544.

[50] D. Walker, B.T. Käsdorf, H.H. Jeong, O. Lieleg, P. Fischer, Enzymatically active biomimetic micropropellers for the penetration of mucin gels, Sci. Adv. 1 (11) (2015) e1500501.

[51] X. Wang, C. Ho, Y. Tsatskis, J. Law, Z. Zhang, M. Zhu, Y. Sun, Intracellular manipulation and measurement with multipole magnetic tweezers, Sci. Rob. 4 (28) (2019) eaav6180.

[52] H. Xie, M. Sun, X. Fan, Z. Lin, W. Chen, L. Wang, Q. He, Reconfigurable magnetic microrobot swarm: multimode transformation, locomotion, and manipulation, Sci. Rob. 4 (28) (2019).

[53] J. Yu, B. Wang, X. Du, Q. Wang, L. Zhang, Ultra-extensible ribbon-like magnetic microswarm, Nat. Commun. 9 (1) (2018) 3260, https://doi.org/10.1038/s41467-018-05749-6.

[54] Z. Yu, D. Dulin, J. Cnossen, M. Köber, M.M. van Oene, O. Ordu, N.H. Dekker, A force calibration standard for magnetic tweezers, Rev. Sci. Instrum. 85 (12) (2014), 123114.

[55] N.A. Zacchia, M.T. Valentine, Design and optimization of arrays of neodymium iron boron-based magnets for magnetic tweezers applications, Rev. Sci. Instrum. 86 (5) (2015), 053704.

[56] L. Zhang, W.F. Dong, H.B. Sun, Multifunctional superparamagnetic iron oxide nanoparticles: design, synthesis and biomedical photonic applications, Nanoscale 5 (17) (2013) 7664–7684.

[57] X. Zhang, L.W. Rogowski, M.J. Kim, Closed-loop control using high power hexapole magnetic tweezers for 3D micromanipulation, J. Bionic Eng. 17 (1) (2020) 113–122.

[58] S. Zhang, X. Hu, M. Li, U. Bozuyuk, R. Zhang, E. Suadiye, M. Sitti, 3D-printed micrometer-scale wireless magnetic cilia with metachronal programmability, Sci. Adv. 9 (12) (2023).

[59] R.N. Zia, Active and passive microrheology: Theory and simulation, Annu. Rev. Fluid Mech. 50 (2018) 371–405.

[60] J.P. Berezney, M.T. Valentine, A compact rotary magnetic tweezers device for dynamic material analysis, Rev. Sci. Instrum. 93 (9) (2022).

[61] S. Le, R. Liu, C.T. Lim, J. Yan, Uncovering mechanosensing mechanisms at the single protein level using magnetic tweezers, Methods 94 (2016) 13–18.

[62] B.M. Lansdorp, S.J. Tabrizi, A. Dittmore, O.A. Saleh, A high-speed magnetic tweezer beyond 10,000 frames per second, Rev. Sci. Instrum. 84 (4) (2013).

[63] V. Bessalova, N. Perov, V. Rodionova, New approaches in the design of magnetic tweezers–current magnetic tweezers, J. Magn. Magn. Mater. 415 (2016) 66–71.

[64] H. Chen, G. Yuan, R.S. Winardhi, M. Yao, I. Popa, J.M. Fernandez, J. Yan, Dynamics of equilibrium folding and unfolding transitions of titin immunoglobulin domain under constant forces, J. Am. Chem. Soc. 137 (10) (2015) 3540–3546.

[65] S. Kim, F. Qiu, S. Kim, A. Ghanbari, C. Moon, L. Zhang, H. Choi, Fabrication and characterization of magnetic microrobots for three-dimensional cell culture and targeted transportation, Adv. Mater. 25 (41) (2013) 5863–5868.